

1

The feasibility of using distributed acoustic sensors in surface seismic application

2 **Samir F. Jreij, Whitney J. Trainor-Guitton, and Jim Simmons**

3 Colorado School of Mines,

4 1500 Illinois Ave,

5 Golden, CO, 80401

6 (April 23, 2018)

7 Running head: **The feasibility of using distributed acoustic sensors in surface seismic
application**

ABSTRACT

9 In this paper, an imaging technique that utilizes sparsely sampled, multi-component geophone data
10 and a dense surface distributed acoustic sensor (DAS) acquisition is proposed. The PoroTomo sur-
11 vey at Brady's Natural Lab consisted of 238 multi-component geophones that are spaced anywhere
12 from 60 meters to 150 meters apart. This proves to be a difficult migration problem with such
13 sparse spacing. Both 2-D and 3-D numerical experiments are performed to test the feasibility of
14 using multi-component geophone and DAS data together. In 2-D, a reflectivity model is created
15 from the local fault model in the PoroTomo Survey. This provided a variety of structural dips to test
16 the imaging technique. It was found that using an horizontal force rather than a vertical force with
17 these models produced a much sharper resulting image. A quantitative analysis is further performed
18 to provide an unbiased perspective on the results. The quantitative analysis utilized both energy
19 norm image filtering and a convolutional neural network to prove that distributed sensors add value
20 to imaging efforts with sparsely-sampled, multi-component geophones. The 2-D example is an ide-

21 alized experiment. A more extreme example is performed in 3-D to confirm the conclusions made
22 in 2-D. A methodology to model DAS data in 3-D is presented prior to showing examples of utiliz-
23 ing the two data types together for imaging. Quantitative analysis is also required for an unbiased
24 perspective on the results. The results from quantitative analysis show that utilizing DAS in surface
25 surveys with a sparse multi-component geophone acquisition proves to be useful in reducing the
26 number of false positives by a small fraction. A more regular experiment must be performed prior
27 to making conclusions about the added value of DAS, so 2-D lines of fiber were utilized instead
28 of the PoroTomo acquisition geometry. The 2-D DAS acquisition increases identifying the true
29 positives significantly.

INTRODUCTION

30 Distributed acoustic sensing (DAS) is a technology that uses Rayleigh scattering in a fiber-optic
31 cable to detect elastic signals when wave particle motion is parallel to the sensing fiber (Hornman
32 et al., 2013). The two main components used in distributed sensing are the interrogator unit and the
33 fiber-optic cable. The interrogator unit works as a light source and receiver. It sends a known pulse
34 of light down the fiber. Nearly any type of existing fiber-optic cable can be used in conjunction
35 with an interrogator unit. Small imperfections within the fiber cause backscattering of light. Strain
36 events along the fiber cause this backscattering to change slightly when a wavefield approaches the
37 fiber. The interrogator unit can measure the Rayleigh backscattering and relate it to the strain along
38 the fiber.

39 **DAS Advantages**

40 DAS has many advantages in various industries. For one, DAS is a low-cost acquisition system
41 in wells that already contain fiber optic cables. Even in those wells that do not already contain
42 fiber optic cables, a DAS vertical seismic profile (VSP) is often more affordable than renting and
43 deploying geophones (Mateeva et al., 2014). DAS also enables seismic surveys to be acquired with
44 dense sampling (as small as 10-centimeter receiver spacing) at large distances (tens of kilometers
45 long). Achieving even 1-meter sampling with conventional geophone is expensive and logically
46 difficult. Lastly, DAS has almost perfect repeatability in 4-D surveys when cemented in a borehole
47 or trenched in the subsurface (Mateeva et al., 2013).

48 **DAS Disadvantages**

49 Although DAS may seem like the solution to seismic acquisition, it also has many disadvantages.
50 DAS is most sensitive to waves that have particle motion parallel to the orientation of the fiber, so
51 it is said that the technology has broadside insensitivity. Multi-component geophones also have this
52 issue; with more recording components, however, they are able to resolve more of the wavefield and
53 are not affected by this broadside insensitivity as much.

54 Another disadvantage is that DAS coupling is not trivial in all environments. In a borehole
55 environment, DAS can be cemented behind casing or permanently installed on production tubing
56 (Mateeva et al., 2013). Surface distributed sensor coupling is a more challenging issue. Lindsey
57 et al. (2017) describe how fibers can be utilized in loosely coupled environments. The Stanford
58 Fiber Optic Array consists of a 2.5 km long array that lies in a conduit about 1 to 2 meters below
59 ground. The DAS fiber geometry is restricted by the conduits, though, and the task of installing the
60 fiber is more difficult if there are no existing conduits. Daley et al. (2013) have trenched the cable
61 and returned at a later time to shoot the seismic survey. Although this method is effective, waiting
62 to shoot a survey at a later time can be inconvenient.

63 **Literature Review**

64 Historically, DAS has been used in a borehole environment for flow monitoring, temperature mea-
65 surements, and vertical seismic profiles (Clarke and Sandberg, 1983; Krohn et al., 2000; Mestayer
66 et al., 2011; Barberan et al., 2012; Cox et al., 2012; Daley et al., 2013; Mateeva et al., 2014).

67 Mestayer et al. (2011) describe how permanently installed fiber-optic infrastructure in existing
68 wells can enable low-cost non-intrusive geophysical monitoring. Geophones generally only acquire
69 data along a short subset of the well. This makes repeatable time-lapse surveys difficult as placing

70 the geophones in the same location is not trivial. Mestayer et al. (2011) also discuss how borehole
71 DAS is able to improve repeatability and time-lapse sensitivity because it is able to acquire data
72 along the full well with a single shot. Mateeva et al. (2014) also describe a time lapse, 3-D DAS
73 VSP application. They conclude that DAS has many major business impacts on fields that require
74 enhanced oil recovery (EOR) including cost efficiency, safety, and synergy with other fiber optic
75 applications.

76 Barberan et al. (2012) discuss different ways DAS fiber can be coupled in a borehole environ-
77 ment. DAS fiber can be clamped to production tubing and used as a downhole seismic sensor.
78 Barberan et al. (2012) expand on this explaining that acquiring seismic data over the entire well is
79 essential for acquiring additional transit times for velocity inversion and it allows for a wide range of
80 incidence angles in terms of wave directions that arrive at the fiber for inversion. Cox et al. (2012)
81 also looks at borehole DAS data, but now for the purpose of imaging. Cox et al. (2012) examine
82 images produced from both geophone and DAS data types in a borehole example. They conclude
83 that images produced from distributed sensing are similar to those produced by geophones and that
84 DAS has potential to replace geophones.

85 Daley et al. (2013) describes field tests from both horizontal and borehole distributed sensors.
86 They conclude that the SNR in surface DAS is not sufficient for observing P-waves and that DAS is
87 more useful in borehole environments or longer surface arrays. They don't go into detail, however,
88 regarding why certain waves are not observable in DAS.

89 As seen in these examples, DAS research has emphasized acquiring data in borehole environ-
90 ments because many wells are already equipped with fiber for production. As a result, acquiring
91 DAS in boreholes is as simple as connecting the existing fiber-optic cable to a new interrogator unit
92 that senses acoustic signal. Although there are some studies on surface DAS acquisitions (Daley

93 et al., 2013; Hornman, 2017), there has not been a thorough study in active source experiments.

94 Most recent papers in DAS fiber focus on how the system can be used independently of geo-
95 phones. This is viable in a borehole environment due to the fact that the predominant particle motion
96 of the recorded seismic data is in the vertical direction, parallel to the fiber. Surface horizontal DAS
97 is sensitive to the horizontal component of particle motion. P-wave reflections will not be recorded
98 on surface DAS at normal incidence, assuming a flat-layered earth, since the particle motion is ver-
99 tical. Daley et al. (2013) experiment with a vibroseis injecting a vertical force source. The reflected
100 P-wave is not recorded on the DAS fiber as the experiment only had 1,000 meters of offset, and,
101 therefore, the authors concluded that the SNR in surface DAS is insufficient for observing P-waves
102 due to the relatively small incidental reflected angle. Other source mechanisms must be investigated
103 before such a conclusion can be made about the feasibility of using surface DAS fiber. Another
104 option is utilizing the DAS fiber with geophones to attempt to minimize the insensitivity of some
105 waves. This paper explores different experiments using the field geometry from the PoroTomo
106 survey in Northwest Nevada and numerical modeling.

107 **PoroTomo Survey**

108 The PoroTomo survey involved four-weeks of data acquisition of geodesy, interferometric syn-
109 thetic aperture radar (InSAR), hydrology, temperature sensing, passive source seismology, and ac-
110 tive source seismology data. These data were jointly collected to characterize and monitor changes
111 in the rock mechanical properties of Brady's Natural Laboratory (BNL), an Enhanced Geothermal
112 System (EGS) reservoir.

113 This paper investigates the active seismic source component of the PoroTomo Experiment. The
114 PoroTomo survey is one of the most unique seismic acquisitions for surface DAS fiber. The survey

115 included 238 multi-component geophones, 156 three-component (vertical and orthogonal horizon-
116 tal) vibroseis source locations that swept from 5 to 80 Hz in 20 seconds, 300 meters of borehole
117 DAS, and nearly nine kilometers of surface fiber-optic cable. The survey geometry is shown in
118 Figure 1.

119 The DAS fiber was placed in a 1-meter deep trench in January of 2016 to settle for the March
120 seismic data acquisition. This is one of the first experiments to allow two months for the fiber to
121 settle. This is also one of the first experiments to investigate the surface DAS sensitivity in 3-D and
122 4-D. BNL has been maintained as a geothermal resource and operated as a power plant by Ormat
123 Technologies for approximately 25 years. During the four-week PoroTomo survey, Ormat operated
124 the geothermal system at different pumping and producing rates in the injection and production
125 wells allowing for a small-scale, time-lapse survey.

126 **Outline**

127 This paper explains, and quantitatively analyzes, different approaches for using surface DAS in
128 active source seismic acquisitions. First, the theory behind DAS fiber and wave types that DAS
129 fiber can record is introduced using theoretical examples. Then, 2-D numerical modeling is utilized
130 to perform a feasibility study on combining DAS and multi-component geophones data to create
131 one image. This is theoretically useful as the multi-component geophones sample the full wavefield
132 (Z, X, and Y components of particle motion) at sparse locations and the DAS fiber samples one
133 component of the wavefield densely. The 2-D examples shown are idealized experiments. More
134 extreme examples must be performed in 3-D prior to making any conclusions with the hypothesis
135 previously presented, so the challenges with modeling DAS are discussed and a numerical modeling
136 example is presented to test if adding DAS data can improve a multi-component DAS image in 3-D.

FIBER SENSITIVITY

137 Understanding how DAS fiber works is essential to working with the data that is currently available
138 and for future surveys. For a conventional DAS seismic survey, a known pulse of light is sent
139 into the fiber using an interrogator unit and some of the light is naturally scattered back due to
140 imperfections within the fiber. The interrogator unit is able to record this scattered light along the
141 fiber up to 10-kilometers away. This is known as the base condition inside of the fiber. The fiber
142 undergoes a strain when a seismic wavefield approaches and a scattering of light is produced that is
143 different from the base condition. The interrogator unit is able to relate this new scattering of light
144 to local strain along the fiber by recording the time of arrival and the phase-lag of the returning light
145 signals (Parker et al., 2014).

146 As stated previously, DAS fiber is most sensitive to waves that are able to stretch and squeeze the
147 fiber, so the waves have to have particle motion parallel to the orientation of the fiber. Every seismic
148 sensor has its own distinct sensitivity to the various types of waves depending on their emergent
149 angle. The emergent angle (θ) represents the angle between the incoming wave and the surface of
150 the Earth. Consider a plane wave reflection in the X-Z plane: an emergent angle of 0° represents
151 a wave arriving parallel to the surface (or a plane wave traveling in the Z-direction); an emergent
152 angle of 90° represents a wave arriving perpendicular to the surface (or a plane wave traveling in
153 the X-direction).

154 These points can be demonstrated with a simple 2-D example. Consider wave propagation
155 in the x-z plane in a homogeneous, flat-layered, isotropic or vertical transverse isotropic medium
156 (Figure 2a-2b). The horizontal DAS fiber is oriented in the x-direction. P-waves have particle
157 motion parallel to the direction of wave propagation (Aki and Richards, 1980). Normal-incidence
158 reflections from a horizontal reflector will arrive perpendicular to the surface fiber. In the case of

159 a 2-D line of horizontal fiber with an vertical vibe, the reflected P-wave will not be seen at short
160 offsets (Figure 2a). The particle motion of P-waves is parallel to the direction of propagation, so
161 at short offsets, the reflected P-wave will arrive perpendicular to the fiber. As seen in Figure 3a,
162 P-waves with a 0° emergent angle show 0 amplitude on fiber and maximum amplitude on the z-
163 component of a geophone. Moving to further offsets yields emergent angles that are at a larger
164 angle to the fiber. According to Figure 3a, these waves will show more data than waves arrive
165 perpendicular to the fiber as they are propagating in the direction of the fiber and less data on the
166 vertical component of the geophone. The further the offset, however, the lower the amplitude of the
167 wave due to attenuation effects.

168 Shear-waves are potentially more interesting when recording with horizontal fiber. Consider
169 again 2-D wave propagation in the x-z plane in a homogeneous, flat-layered, isotropic or vertical
170 transverse isotropy medium (Figure 2b). SV-waves have particle motion in the x-z plane, as do
171 P-waves (Aki and Richards, 1980). Normal-incidence reflections from a horizontal reflector will
172 arrive perpendicular to the surface fiber. P-wave particle motion, as stated previously, will be in the
173 z direction, and consequently, will not be recorded by the fiber. SV wave particle motion will be
174 in the x-direction (emergent angle of 0°), and the DAS response will be maximum (Figure 3b). At
175 larger offsets, the SV-wave emerging angle begins to approach 90° . A larger emerging angle means
176 less signal (Figure 3b) is recorded by both the surface DAS and the x-component of the geophone
177 because the SV-wave particle motion approaches perpendicular to these components (Figure 2b).

178 We also consider using SH-waves with the same 2-D survey geometry (homogeneous, flat-
179 layered, isotropic). SH-waves propagate in the x-z plane. SH waves have particle motion perpendic-
180 ular to the direction of wave propagation or, in this case, in the y-direction. The SH-DAS response
181 will be zero since the SH particle motion is perpendicular to the DAS fiber in the y-direction. In
182 this 2-D case, the SH-wave will be out of plane regardless of source-receiver offset. In 3-D, SH-

183 waves can be seen on the DAS if they are properly oriented. For example, a source-receiver azimuth
184 perpendicular to the 2-D fiber (in this case, in the y-direction) will produce a maximum amplitude
185 reflection on the DAS since the particle motion is in the x-direction for all offsets. As the source-
186 receiver azimuth moves inline with the fiber, the SH-wave particle motion decreases, and is equal
187 to zero when the source-receiver azimuth is inline with the fiber.

2-D NUMERICAL MODELING EXAMPLES

188 Imaging the geophone data is a difficult task in the PoroTomo Survey due to the irregular spatial
189 sampling and offset. This paper focuses on identifying a way to resolve the spatial sampling issue.
190 Fortunately, the PoroTomo survey includes surface DAS cable that has 10-meter gauge-length and
191 an equivalent of 1-meter receiver spacing along the fiber. Many papers in the literature are interested
192 in methods to convert DAS measurements (strain or strain rate) to a geophone equivalent (particle
193 velocity or displacement) with the intent to replace point sensors with distributed sensors, or use
194 existing geophone processing to clean up DAS data (Daley et al., 2013, 2015; Jreij et al., 2017).
195 The idea of using both data types in simultaneous imaging is explored in this paper to produce more
196 detailed images using synthetic examples.

197 2-D Synthetic Design

198 Siler and Faulds (2013) mapped the faults of Brady's Natural Lab shown in Figure 4. It is important
199 to image these faults in detail as they are driving factors behind the recharge of the geothermal
200 reservoir (Feigl, 2017; Folsom et al., 2018). For this reason, a slice is taken from one of the wells
201 Brady's Natural Lab (Siler and Faulds, 2013) in the PoroTomo Survey are used as reflection velocity
202 models. This slice is shown in Figure 5. The Siler and Faulds (2013) fault model is used as a

203 reflectivity model as it contains a variety of structural dips. It is important to test the structural dip
204 imaging extremes with new methods to see how they will work in complicated subsurfaces.

205 Seismic sources in the PoroTomo experiment are not on a uniform grid. In fact, the source
206 spacing is as large as 150 meters. The aim of this paper is to discuss how DAS and multi-component
207 geophones can be used together to create a more detailed image. Seismic illumination describes
208 how much of the subsurface can be imaged given a source-receiver geometry and velocity model.
209 Illumination in seismic surveys is highly influenced by source-receiver spacing. For the purpose of
210 this section, a constant source spacing of 75 meters (which is about the average source spacing in
211 the PoroTomo survey) is used to minimize migration artifact effects from poor illumination. A 20
212 Hz Ricker wavelet is utilized at every source location. As discussed in the previous section, certain
213 wave reflections are better for surface DAS experiments. Different sources will cause different
214 reflection event amplitudes and directions. For the 2-D experiments present in this paper, both
215 vertical and horizontal force sources are modeled.

216 2-D elastic forward modeling is used to produce strain and displacement data along the surface
217 of our 2-D example excited by a vertical force source. Receivers at every one meter across the
218 experiment are used for recording. This represents a 1,500 meter long, 2-D surface DAS line. As
219 seen in Figure 1, the PoroTomo survey did not include a straight fiber that was this long. Instead,
220 the fiber was placed in an attempt to capture a variety of reflection data azimuths. It did include,
221 however, a maximum offset of 1,500-meters across the entire survey. For this reason, this whole
222 offset is included for the 2-D example.

223 The code generated for these experiments outputs both strain and displacement at every receiver
224 location. Receivers are recorded originally at every one meter across the experiment. The geophones
225 are not sampled every one meter in the PoroTomo survey. The average geophone spacing of about

226 70 meters. A geophone spacing of 100 meters is chosen to analyze geophone spacing closer to the
227 extremes of this experiment. The data are generated from a reflectivity model that is derived from
228 Brady's fault model using an elastic FDM operator from the Madagascar package (Fomel et al.,
229 2013). The next step is to back propagate the recorded data from this forward modeling to recover
230 the receiver wavefield. If this was a field experiment, the field data would be back propagated. The
231 adjoint elastic operator is utilized rather than the forward elastic operator to obtain a more exact
232 solution to the imaging problem. Two different sources are needed to create the receiver wavefield.
233 An acceleration force is used for back propagation of the geophone data and a stress tensor is used
234 for back propagation of the DAS data. The proper way to do imaging is to back propagate the
235 data simultaneously, but this was not possible with current codes, so the data are back propagated
236 individually.

237 The last wavefield that needs to be generated is the source wavefield. The source wavefield is a
238 forward model from the original source location through a smooth velocity model. It is important
239 that the velocity model is smooth as reflections will cause an improper final image. Now, a source
240 and two receiver wavefields exist. An imaging condition is required to combine the wavefields.

241 Traditionally, the zero-lag, cross correlation imaging condition (IC) is used to create a migrated
242 image (Claerbout, 1985). Although this methodology may provide a solution for elastic imaging,
243 this IC produces four resulting images (PP, PS, SP, SS). This proves to be a more difficult com-
244 parison between different data types for the purpose of this paper. Rocha et al. (2016) describes
245 the use of an energy-norm based IC that exploits wavefield directionality to create one final elas-
246 tic image that represents the measure of reflected energy. There are many other benefits to using
247 the energy-norm IC, but the key is that one final image allows for an easy comparison of migrated
248 elastic data.

249 The image produced from the elastic energy norm RTM with sparsely sampled multi-component
250 geophones is shown in Figure 6a. This image shows reflectors are discontinuous and difficult to fol-
251 low. The image is also covered with migration artifacts due to insufficient sampling of the wavefield.
252 An example of this is presented around 800 meters on the x-axis of Figure 6a: the migration artifacts
253 make it difficult for an interpreter to follow the shallow reflector. The deeper reflector in Figure 6a
254 is impossible to identify.

255 The image produced from the elastic energy norm RTM with DAS fiber along the surface of the
256 model creating a virtual receiver at every one meter is shown in Figure 6b. The shallow reflector in
257 this image is sharp and continuous, allowing for easy interpretation. Although migration artifacts
258 are still present around 800 meters on the x-axis, these are different from those experienced in
259 Figure 6a. These migration artifacts are now due to fake modes present because the wavefield is
260 extrapolated using only the x-component data that was recorded with DAS fiber.

261 Now there are two images with two different migration artifacts (i.e. types of noise). The power
262 of stacking the images should theoretically reduce the noise and highlight the reflection events.
263 Linearly stacking the events, however, will not currently work as the amplitudes are on different
264 scales. Instead, the amplitudes of both images are normalized by the maximum and then stacked to
265 produce Figure 6c. Although Figure 6c still has artifacts in it, the reflectors are enhanced and the
266 image is easier to interpret than Figure 6a or Figure 6b.

267 **Value of Information**

268 All of the experiments presented in the paper can be qualitatively analyzed and discussed, but quali-
269 tative analysis is always different between people due to different biases and perspectives. A method
270 to quantitatively analyze the experiments is needed to do effective comparisons.

271 The Value of Information (VOI) is a quantitative tool that originates from the field of decision
 272 analysis to quantify how relevant and reliable an information source is (Trainor-Guitton et al., 2013).
 273 VOI estimates the possible increase in expected utility by gathering information. It is calculated by
 274 subtracting the prior value (V_{prior}) from the value with imperfect information ($V_{imperfect}$) shown in
 275 Equation 1.

$$VOI = V_{imperfect} - V_{prior} \quad (1)$$

276 The goal of this project is to observe if there is any added value to using distributed acoustic
 277 sensing in surface acquisitions. The value with imperfect information shown in Equation 2 can only
 278 be calculated with a quantitative measure of how accurate the information source is.

$$V_{imperfect} = \sum_{j=F,NF} Pr(\theta^{int} = \theta_j) \max_a \left[\sum_{i=F,NF} Pr(\theta = \theta_i | \theta^{int} = \theta_j) v_a(\theta_i) \right] \quad (2)$$

279 This quantitative measure can be represented by the posterior probability, $Pr(\theta = \theta_i | \theta^{int} = \theta_j)$,
 280 of the value with imperfect information equation 2. Specifically for these problems, the posterior
 281 probability can be how often interpretations of faults align with the actual presence of faults. It is im-
 282 portant to calculate the posterior reliability so the value of imperfect information can be completed.
 283 The posterior probability can be calculated using Equation 3,

$$Pr(\theta = \theta_i | \theta^{int} = \theta_j) = \frac{(Pr(\theta = \theta_i)) Pr(\theta^{int} = \theta_j | \theta = \theta_i)}{Pr(\theta^{int} = \theta_i)}; \forall i, j = F, NF \quad (3)$$

284 where θ represents a true value of Fault or Not Fault, θ^{int} represents an interpreted Fault or Not
 285 Fault. There are a variety of methodologies to produce information about whether an interpreted

286 fault is actually a fault or not. The two that are utilized in this paper are energy filtering and machine
287 learning.

288 *Energy Filtering*

289 As discussed previously in this paper, the resulting image from energy norm reverse time migration
290 represents the relative amount of energy reflected in the subsurface. All images are simply a matrix
291 of these relative reflected energy values. In theory, the largest amplitudes from this image will
292 be reflection events. In the case of this experiment, the reflection events represent the fault plane
293 targets of imaging. An amplitude filter is used as a first pass to interpret reflections in the dataset to
294 calculate the posterior distribution.

295 Every model cell that is above the applied limit is assigned a value of 1 and every model box
296 that is below the limit is assigned a value of 0. For example, the image in Figure 6a shows that
297 the maximum absolute amplitude is about 500,000. The top 80%, 90% and 95% of the reflected
298 energy are filtered on the image to highlight areas where reflections are coming from as opposed
299 to migration artifacts. The results are shown in Figure 7 for the top 90% of the reflected energy.
300 Although the results in Figure 7 are not perfect representations of where interpreters would place
301 the faults, this approach represents the beginning steps to quantify the value added by DAS fiber
302 with sparse multi-component geophones.

303 A cell-by-cell comparison between the filtered energy images (Figure 7) and the original fault
304 image (Figure 5) is performed to identify how accurate both technologies are able to identify features
305 in the fault model. The results of this cell-by-cell comparison are presented in confusion matrix form
306 (Table 1). A confusion matrix is a table that describes performance on a set of test data for which
307 the true value is known. The term θ_F denotes that an actual fault exists and the term θ_{NF} denotes

Table 1: Confusion matrix for top 90% energy reflected.

Top 90% energy reflected		
	θ_F^{int}	θ_{NF}^{int}
θ_F	307	336
θ_{NF}	922	21685

308 that no fault exists. The terms θ_F^{int} and θ_{NF}^{int} represent the interpretations of fault and no fault,
 309 respectively, based on energy filtering of images. The columns of the confusion matrix represent
 310 predicted classifications (θ_F^{int} and θ_{NF}^{int}). The rows of the confusion matrix represent actual true
 311 statement of the subsurface (θ_F and θ_{NF}).

312 The confusion matrices assist in calculating the posterior value using Equation 3. The posterior
 313 value gives the probability that an event which the data type predicted is the event present. The
 314 posterior can then be used to calculate the utility or value of information added when using DAS and
 315 geophone versus only geophone with Equation 1. The results for the posterior values are displayed
 316 graphically in Figure ?? for the vertical source. In every experiment, adding distributed sensors
 317 increases the probability of finding if a cell is a fault or not a fault (true positive or a true negative)
 318 and decreases the probability of a cell being a false positive or false negative.

319 Energy norm imaging allowed for an automatic method to interpret images output from the
 320 migration images. Filtering images based on amplitudes, however, is a crude approximation of
 321 how an interpreter would “interpret” an image. A more sophisticated method to interpret images
 322 is required to get a better quantitative analysis of the imaging technique, so a machine learning
 323 classification scheme is examined.

324 *Convolutional Neural Network Analysis*

325 Machine learning is a field within computer science that focuses on the ability of computer systems
326 to learn patterns within data without being explicitly programmed for these patterns (Samuel, 1959).
327 Machine learning has had a large boom in the geophysics industry within the last 10 years. The rea-
328 sons for this are quite apparent: geophysicist work with large amounts of data, the geophysics field
329 needs more quantitative analysis rather than qualitative, and machines are much better at identifying
330 weak or high-dimensional patterns than humans are.

331 There are a variety of machine learning algorithms that can be utilized based on the problem that
332 needs to be solved. One of the most powerful machine learning algorithms is the neural network.
333 Neural networks are inspired by the biological neural networks that constitute human brains or at
334 least how humans perceive they work (Gerven and Bohte, 2018). They consist of many layers in
335 parallel and every layer consists of a number of nodes. All neural networks consist of at least two
336 layers: the input layer and output layer. All the extra layers in between the input and output layers
337 are the hidden layers. The nodes of every layer are like neurons in the brain. Every neuron has its
338 own activation function that determines whether it should be “fired” or not similar to how a neuron
339 in the brain behaves. Each layer receives the output from the previous layer based on if the previous
340 neuron is fired or not.

341 Convolutional Neural Networks (CNN) in particular are at the core of most state-of-the-art com-
342 puter vision solutions for a wide variety of tasks. One of the most accurate CNN image classifiers
343 is the Inception-v3 model (Szegedy et al., 2015). The original Inception-v3 model is trained and
344 tested on the 2012 ImageNet Large Scale Visual Recognition Challenge (Russakovsky et al., 2015).
345 The training dataset consisted of 10,000,000 labeled images that depicted 1,000 object categories.
346 The Inception-v3 model was able to perform with 3.5% top-5 error, meaning that the target label

347 is within the top-5 probability classifications that the algorithm produced. A top-5 error of 3.5%
348 means the Inception-v3 model is able to perform with high accuracy, making it a top contender for
349 a geophysics image classification problem.

350 The Inception-v3 model utilizes transfer learning which means it stores knowledge gained from
351 training on the ImageNet dataset and then applies it to a different but related problem. It is difficult
352 to train a CNN from scratch because a large dataset is needed with a substantial amount of machines
353 equipped with GPU's. Instead, the intermediate layers of the Inception-v3 model are used as they
354 are already trained on detecting edges, shapes, and other high level features. The last layer of the
355 model is retrained to identify if an image is either a fault or not a fault.

356 Figure 8 shows the architecture of one module in the Inception v3 model. The full architecture
357 has a large amount of modules similar to the one shown in Figure 8 that decompose the image into
358 smaller subsets and apply different filters. Some of these subsets can be as small as one pixel by
359 one pixel, while others are as large as the image size.

360 Within each image, there are a variety of features that contribute to the final classification.
361 It is not feasible for the algorithm to identify these features using pixel by pixel methodologies.
362 Instead, pooling allows for a smaller subset of the image to be analyzed for a certain statistic such
363 as mean, maximum, or minimum. Strides in the convolutional neural network world are how much
364 the filter that the network is applying is shifted. After learning a certain portion of the image,
365 the network must perform a stride to get to the next location. These strides are important when
366 analyzing a variety of images as they dictate the search area. Convolutional layers perform filtering
367 operations on the image or combine two images that have been filtered previously. One way to
368 apply convolution is in the sense of an edge detector: the original image is convolved with a kernel
369 matrix that represents an edge filter. Inception-v3 utilizes convolutional layers like the edge filter to

370 identify patterns within images.

371 The Inception v3 model's ability to identify features can be leveraged within the geophysics
372 realm. The first step is to create some training data to retrain the model. The objective is to see
373 if DAS helped identify more faults than a sparse array of multi-component geophones. For the
374 experiments in this chapter, RTM images are created from 2-D reflectivity slices of the Siler and
375 Faulds (2013) fault model. There are about 500 other slices along both the X and Y axis of the
376 PoroTomo grid. A number of these slices can be migrated to create training data for identifying
377 faults.

378 The next step is to take windows of the migrated images and label them based on if there are
379 faults or not within the image. 100 meter by 100 meter (10 grid cell by 10 grid cell) subsets of the
380 migrated images were created. There are a large amount of data present and individually picking
381 whether an image contains a fault or not would take a long time. As stated earlier, the true fault
382 model exists to compare with the migrated images. The same subset of the migrated images can
383 be compared with the reflectivity model. If more than half the pixels are a fault, then the program
384 labels the training data as a fault (Figure 9a). Otherwise, the program labels the training data as not
385 a fault (Figure 9b).

386 This is an easy and automatic way to generate training data, but training is an essential step
387 prior to testing, so it needs to be continually improved. The next step is to QC the training data to
388 make sure that the examples are actually of "faults" and "not faults". There is a lot of back and forth
389 until an acceptable cross-validation accuracy is achieved. A total of 2500, 100 meter by 100 meter
390 windowed RTM images were used to train the CNN to detect faults. A final training validation
391 accuracy of 94.4% is achieved. This is an acceptable accuracy check and now the neural network is
392 ready to be tested on data that were not included in the training data.

Table 2: Confusion matrices for CNN created from the geophones (Figure 6a) and both data types together (Figure 6c) using a vertical force source.

Multicomponent Geophone			DAS & Geophone		
	θ_F^{int}	θ_{NF}^{int}		θ_F^{int}	θ_{NF}^{int}
θ_F	292	1008		θ_F	420
θ_{NF}	327	1998		θ_{NF}	199
					1176

393 A 100 meter by 100 meter testing data is created the same way the training data is created. The
 394 testing data is kept hidden from the training data. The first RTM image that is used for testing is the
 395 vertical source data from the velocity model shown in Figure 5. The first test is on the sparse, multi-
 396 component geophone image (Figure 6a). The RTM image is decomposed into 3,625 (100 meter x
 397 100 meter) images with labels of “Faults” and “Not Faults”. A confusion matrix is then calculated
 398 by evaluating the predictions to the actual fault or no fault classifications of the test data. This same
 399 process is used for the synthetic created from DAS and multi-component geophones. The results of
 400 these experiments are shown in Table 2.

401 Now that a confusion matrix of results is available, a posterior reliability of information can
 402 be calculated just as it was completed for the energy norm filtered images. The resulting posterior
 403 reliability of information is shown in Table 3.

404 The results from Table 3 for the vertical source shows that adding DAS into the sparse array of
 405 geophones with 5 as the velocity model improves the classification of faults by 20%. However, there
 406 is an increase in false negatives by about 30%. This means either the normalized, stacked image
 407 has many artifacts or the classifier needs to be better trained on what is not a fault. The number of
 408 false positives decreases by 20% which is a substantial amount. Lastly, the number of true negatives
 409 decreases by almost 30%. This confirms that the classifier needs to be better trained on what is not
 410 a fault.

Table 3: Posterior reliability of information from CNN calculated using Equation 3 using a vertical force source with Figure 5 as the velocity model.

	Vertical Source Geophone	Vertical Source Geophone & DAS
$Pr(\theta = \theta_F \theta^{int} = \theta_F)$	47.17 %	67.85 %
$Pr(\theta = \theta_F \theta^{int} = \theta_{NF})$	33.53 %	61.39 %
$Pr(\theta = \theta_{NF} \theta^{int} = \theta_F)$	52.83 %	32.14 %
$Pr(\theta = \theta_{NF} \theta^{int} = \theta_{NF})$	66.47 %	38.61 %

411 Although it was overtrained on true faults, the CNN classifier does a much better job at classi-
 412 fying an image than energy norm filter. The false positives and false negatives will decrease with
 413 more training iterations especially in training the classifier on images that are not faults.

414 **Summary**

415 This section discussed in great detail how 2-D DAS data can be modeled. It also showed how a long
 416 offset, 2-D surface DAS line can produce a sharp resulting image. A quantitative analysis using two
 417 methodologies showed that DAS does add value to sparse geophone arrays. This hypothesis must
 418 now be confirmed with a 3-D acquisition.

3-D NUMERICAL MODELING EXAMPLES

419 The objective of this paper is to observe if there is any added value of using surface DAS with
 420 sparsely sampled, multi-component geophones. In the previous section, we observed that in a long
 421 2-D line, there is added value using DAS to help with the spatial sampling. In 3-D, however, there
 422 are many more complications than in 2-D. This section explores additional examples of using DAS

423 in combination with multi-component geophones, but now with the PoroTomo 3-D survey geometry.

424 These examples utilize numerical modeling to understand more about what is recorded.

425 A velocity model is needed to create data. There are a few velocity models to choose from at

426 Brady's Natural Lab: a 1-D interval velocity model from borehole DAS, a model created from body

427 wave tomography (Thurber et al., 2017), and a model from sweep interferometry (Matzel et al.,

428 2017a). Figure 10 shows a comparison between all these velocity models extracted at Well 56-1A.

429 There is a lot of uncertainty between these three velocity models due to the method used to

430 create them. Slow velocities disrupt the finite difference stability condition, so the velocity model

431 from Matzel et al. (2017a) shown in Figure 11 was used for the 3-D modeling.

432 As in the previous section, a modified version of the conventional elastic FDM code (ewefdm)

433 present in Madagascar (Fomel et al., 2013) is utilized, but now for the 3-D case. This allows us to

434 recover both displacement and strain data along receivers in the grid. A variable density is now used

435 to create reflectivity instead of using purely velocity changes to create reflectivity in the 2-D case.

436 **3-D Modeling of Non-Uniform DAS Acquisition**

437 The wavefield along the fiber is now recorded for the six components of strain (XX, XY, XZ, YY,

438 YZ, and ZZ). Field DAS data with single fiber, however, does not recover all six components. In-

439 stead, it only recovers contributions of the wavefield in the direction that it is oriented. We can

440 project the six components from the synthetic data on to the vector direction of the field fiber loca-

441 tions to recover the strain in the direction that the fiber is oriented by using Equation 4,

$$\begin{bmatrix} \varepsilon_{ZZ} \\ \varepsilon_{XX} \\ \varepsilon_{YY} \\ \varepsilon_{XY} \\ \varepsilon_{YZ} \\ \varepsilon_{ZX} \end{bmatrix} = \begin{bmatrix} V_Z^2 & V_X^2 & V_Y^2 & 2V_XV_Y & 2V_YV_Z & 2V_ZV_X \end{bmatrix} = \begin{bmatrix} \varepsilon' \end{bmatrix} \quad (4)$$

442 where ε_{ij} is the strain in the direction ij , V_i is the vector projection in the i direction, and ε' is
 443 the strain in the direction of the fiber.

444 A matrix of fiber vector directions must be created prior to using Equation 4. The fiber endpoints
 445 were recorded in the field using a handheld GPS device after the fiber was trenched. The virtual
 446 receiver locations along the fiber were then interpolated at 1-meter spacing between these endpoints.
 447 Although this gives a good estimate of the x and y coordinates of the fiber, this does not give any
 448 information on how deep the fiber was trenched. For this reason, we assume that the fiber was
 449 all trenched in the same horizontal plane and there are no dips along the fiber. This simplifies
 450 Equation 4 to only have contributions from X and Y. We can then create a plot of these vector
 451 directions shown in Figure 12.

452 Applying Equation 4 recovers only one value of strain along the fiber. In reality, there are
 453 contributions from both X and Y, so the strain matrix should have values at XX, YY, and XY. We
 454 can use the adjoint operation to recover a vector projection of the strain value from Equation 4. The
 455 adjoint operation shown in Equation 5 returns back to the original PoroTomo coordinate system.

$$\begin{bmatrix} \varepsilon' \\ V_Z^2 \\ V_X^2 \\ V_Y^2 \\ 2V_X V_Y \\ 2V_Y V_Z \\ 2V_Z V_X \end{bmatrix} = \begin{bmatrix} \varepsilon_{ZZ} \\ \varepsilon_{XX} \\ \varepsilon_{YY} \\ \varepsilon_{XY} \\ \varepsilon_{YZ} \\ \varepsilon_{ZX} \end{bmatrix} \quad (5)$$

456 The last attribute of fiber that needs to be modeled is the gauge-length. As discussed in Chap-
 457 ter ??, the gauge-length of fiber is related to the wavelength recorded along the fiber and it acts as
 458 a moving average. The gauge-length in the PoroTomo survey was set at 10-meters, so the modeled
 459 data, d , is a matrix multiplication of $\frac{1}{10}$ for the gauge length, the spatial sampling 1-meter, and the
 460 raw point data, b , recorded by the finite difference code (shown in Equation 6, modified from Lim
 461 Chen Ning and Sava, 2018).

462 The last attribute of fiber that needs to be modeled is the gauge-length. As discussed in earlier
 463 in this paper, the gauge-length of fiber is related to the wavelength recorded along the fiber and it
 464 acts as a moving average. The gauge-length in the PoroTomo survey was set at 10-meters, so the
 465 modeled data, d , is a matrix multiplication of $\frac{1}{10}$ for the gauge length, the spatial sampling 1-meter,
 466 and the raw point data, b , recorded by the finite difference code (shown in Equation 6, after Lim
 467 Chen Ning and Sava, 2018).

$$\begin{bmatrix} d_5 \\ d_6 \\ d_7 \\ \vdots \\ d_{n-5} \end{bmatrix} = \frac{1}{10} \begin{bmatrix} 1 & 1 & 1 & 1 & 1 & 1 & 1 & 1 & 1 & 1 & 0 & 0 & 0 & 0 \\ 0 & 1 & 1 & 1 & 1 & 1 & 1 & 1 & 1 & 1 & 1 & 0 & 0 & 0 \\ 0 & 0 & 1 & 1 & 1 & 1 & 1 & 1 & 1 & 1 & 1 & 1 & 0 & 0 \\ 0 & 0 & 0 & \ddots & 0 \\ 0 & 0 & 0 & 0 & 1 & 1 & 1 & 1 & 1 & 1 & 1 & 1 & 1 & 1 \end{bmatrix} \begin{bmatrix} b_5 \\ b_6 \\ b_7 \\ \vdots \\ b_{n-5} \end{bmatrix} \quad (6)$$

468 The DAS data are now ready to be modeled as they are recorded in the real world after all of the
 469 steps described in this section.

470 **Numerical Modeling**

471 The first step in the synthetic is to generate data. The data is generated from a reflectivity model.
 472 The reflectivity in this experiment is caused by the density contrast in the model subsurface. The
 473 variable density, elastic FDM operator is used to propagate a wavefield through the reflectivity
 474 model from a given source location. The strain data is recorded along the fiber and the displacement
 475 data is recorded at the geophones.

476 The next step is to create a receiver wavefield. The receiver wavefield is conventionally re-
 477 covered by back propagating the recorded field data. In the case of this numerical experiment, the
 478 data that were synthetically generated from a reflectivity model are back propagated. The data are
 479 reversed in time, reinjected at all the receiver points, and propagated using the forward elastic oper-
 480 ator. Again, two different sources are needed to create the receiver wavefield. An acceleration force
 481 source is used for back propagation of the geophone data and a stress tensor source is used for back
 482 propagation of the DAS data. There is no current way to explode both sources at the same time

483 in the Madagascar package. Instead, two different receiver wavefields are created for the DAS and
484 geophone data. Now, a source and two receiver wavefields exist. An imaging condition is required
485 to combine the two wavefields.

486 The 2-D section first discusses the option of using the conventional imaging condition by Claer-
487 bout (1985) which involves taking the zero-lag, cross correlation at each time step for every experi-
488 ment. This IC can be extended into 3-D space with the additional y-component of the wavefield. It
489 is difficult to make comparisons with all of the images that come out of the conventional elastic IC.
490 Instead, the energy norm IC is utilized to produce one final image that does not require wavefield
491 separation (Rocha et al., 2016).

492 It is important to image the faults in detail at Brady's Natural Lab as they are the driving factors
493 behind the recharge of the geothermal reservoir. Although Siler and Faulds (2013) would be a good
494 candidate for data modeling, a simpler model is needed to first test the hypothesis of imaging using
495 the two data types simultaneously. A four layer model with a variety of structures is used as the
496 density model for the first example (Figure 13). There is a contrast of about 300 g/cc between each
497 layer to ensure strong reflections.

REFERENCES

- 498 Aki, K., and P. G. Richards, 1980, Quantative seismology: Theory and methods: New York, **801**.
- 499 Barberan, C., C. Allanic, D. Avila, J. Hy-Billiot, A. Hartog, B. Frignet, and G. Lees, 2012, Multi-
- 500 offset seismic acquisition using optical fiber behind tubing: Presented at the 74th EAGE Confer-
- 501 ence and Exhibition incorporating EUROPEC 2012.
- 502 Claerbout, J. F., 1985, Imaging the earth's interior: Blackwell scientific publications Oxford, **1**.
- 503 Clarke, R., and C. L. Sandberg, 1983, Fiber optic temperature sensing. (US Patent 4,417,782).
- 504 Cox, B., P. Wills, D. Kiyashchenko, J. Mestayer, J. Lopez, S. Bourne, R. Lupton, G. Solano, N.
- 505 Henderson, D. Hill, et al., 2012, Distributed acoustic sensing for geophysical measurement, mon-
- 506 itoring and verification: **37**, 7–13.
- 507 Daley, T., D. Miller, K. Dodds, P. Cook, and B. Freifeld, 2015, Field testing of modular borehole
- 508 monitoring with simultaneous distributed acoustic sensing and geophone vertical seismic profiles
- 509 at citronelle, alabama: Geophysical Prospecting.
- 510 Daley, T. M., B. M. Freifeld, J. Ajo-Franklin, S. Dou, R. Pevzner, V. Shulakova, S. Kashikar, D. E.
- 511 Miller, J. Goetz, J. Henninges, et al., 2013, Field testing of fiber-optic distributed acoustic sensing
- 512 (das) for subsurface seismic monitoring: The Leading Edge, **32**, 699–706.
- 513 Feigl, K. L., 2017, Overview and preliminary results from the porotomo project at brady hot springs,
- 514 nevada: Poroelastic tomography by adjoint inverse modeling of data from seismology, geodesy,
- 515 and hydrology: Presented at the Stanford Geothermal Workshop.
- 516 Folsom, M., J. Lopeman, D. Perkin, and M. Sophy, 2018, Imaging shallow outflow alteration to
- 517 locate productive faults in ormats bradys and desert peak fields using csamt.
- 518 Fomel, S., P. Sava, I. Vlad, Y. Liu, and V. Bashkardin, 2013, Madagascar: Open-source software
- 519 project for multidimensional data analysis and reproducible computational experiments: Journal
- 520 of Open Research Software, **1**.

- 521 Gerven, M. V., and S. Bohte, 2018, Artificial Neural Networks as Models of Neural Information
522 Processing.
- 523 Hornman, J., 2017, Field trial of seismic recording using distributed acoustic sensing with broadside
524 sensitive fibre-optic cables: *Geophysical Prospecting*, **65**, 35–46.
- 525 Hornman, K., B. Kuvshinov, P. Zwartjes, and A. Franzen, 2013, Field trial of a broadside-sensitive
526 distributed acoustic sensing cable for surface seismic: Presented at the 75th EAGE Conference
527 & Exhibition incorporating SPE EUROPEC 2013.
- 528 Jreij, S., W. Trainor-Guitton, D. Miller, et al., 2017, Field data comparison of 3d horizontal dis-
529 tributed acoustic sensing and geophones: SEG Technical Program Expanded Abstracts.
- 530 Krohn, D. A., T. MacDougall, and A. Mendez, 2000, Fiber optic sensors: fundamentals and appli-
531 cations: Isa.
- 532 Lindsey, N. J., E. R. Martin, D. S. Dreger, B. Freifeld, S. Cole, S. R. James, B. L. Biondi, and J. B.
533 Ajo-Franklin, 2017, Fiber-optic network observations of earthquake wavefields: *Geophysical*
534 *Research Letters*.
- 535 Mateeva, A., J. Lopez, J. Mestayer, P. Wills, B. Cox, D. Kiyashchenko, Z. Yang, W. Berlang, R.
536 Detomo, and S. Grandi, 2013, Distributed acoustic sensing for reservoir monitoring with vsp:
537 *The Leading Edge*, **32**, 1278–1283.
- 538 Mateeva, A., J. Lopez, H. Potters, J. Mestayer, B. Cox, D. Kiyashchenko, P. Wills, S. Grandi, K.
539 Hornman, B. Kuvshinov, et al., 2014, Distributed acoustic sensing for reservoir monitoring with
540 vertical seismic profiling: *Geophysical Prospecting*, **62**, 679–692.
- 541 Matzel, E., X. Zeng, C. Thurber, Y. Luo, C. Morency, et al., 2017a, Seismic interferometry using
542 the dense array at the brady geothermal field.
- 543 Matzel, E. M., X. Zeng, C. Thurber, and C. Morency, 2017b, Using Virtual Earthquakes to Charac-
544 terize the Material Properties of the Brady Hot Springs , Nevada: Geothermal Resources Council.

- 545 Mestayer, J., B. Cox, P. Wills, D. Kiyashchenko, J. Lopez, M. Costello, S. Bourne, G. Ugueto,
546 R. Lupton, G. Solano, et al., 2011, Field trials of distributed acoustic sensing for geophysical
547 monitoring, *in* SEG Technical Program Expanded Abstracts 2011: Society of Exploration Geo-
548 physists, 4253–4257.
- 549 Parker, T., S. Shatalin, and M. Farhadiroushan, 2014, Distributed Acoustic Sensing - A new tool for
550 seismic applications: *First Break*, **32**, 61–69.
- 551 Rocha, D., N. Tanushev, and P. Sava, 2016, Isotropic elastic wavefield imaging using the energy
552 norm: *Geophysics*, **81**, S207–S219.
- 553 Russakovsky, O., J. Deng, H. Su, J. Krause, S. Satheesh, S. Ma, Z. Huang, A. Karpathy, A. Khosla,
554 M. Bernstein, A. C. Berg, and L. Fei-Fei, 2015, ImageNet Large Scale Visual Recognition Chal-
555 lenge: *International Journal of Computer Vision (IJCV)*, **115**, 211–252.
- 556 Samuel, A. L., 1959, Some studies in machine learning using the game of checkers: *IBM Journal*
557 of research and development
- 558 **3**, 210–229.
- 559 Siler, D. L., and J. E. Faulds, 2013, Three-dimensional geothermal fairway mapping: Examples
from the western great basin, usa,: *GRC Transactions*, **7**, 327–332.
- 560 Szegedy, C., V. Vanhoucke, S. Ioffe, J. Shlens, and Z. Wojna, 2015, Rethinking the Inception Ar-
561 chitecture for Computer Vision.
- 562 Thurber, C., X. Zeng, L. Parker, et al., 2017, Active-source seismic tomography at bradys geother-
563 mal field, nevada, with dense nodal and fiber-optic seismic arrays: *American Geophysical Union*.
- 564 Trainor-Guitton, W. J., A. Ramirez, X. Yang, K. Mansoor, Y. Sun, and S. Carroll, 2013, Value
565 of information methodology for assessing the ability of electrical resistivity to detect co2/brine
566 leakage into a shallow aquifer: *International Journal of Greenhouse Gas Control*, **18**, 101–113.

LIST OF FIGURES

567 1 PoroTomo survey geometry. Green dots represent source locations, red dots represent geo-

568 phone locations, and the blue line represents the surface DAS layout.

569 2 Consider a source that generates both P and S waves; this is a 2-D Homogeneous, flat-

570 layered, isotropic ray path example. The blue lines represent ray paths of the labeled waves, the

571 blue arrow represents the propagation direction of the wave, the green line represents a horizontal

572 reflector in the subsurface, and the yellow star represents the source. (a) Demonstration of P-P wave

573 effect on fiber using ray paths. Particle motion is inline with propagation direction (blue arrow).

574 The fiber will only record data at large offsets. (b) Demonstration of P-SV wave effect on fiber

575 using ray paths. Particle motion is perpendicular with the propagation direction (green arrows). The

576 fiber will only record data at short offsets.

577 3 Amplitude versus emerging angle for both geophone (blue) and horizontal DAS (red). An

578 emerging angle of 0° indicates a wave that is propagating perpendicular to the surface and an emerg-

579 ing angle of 90° degrees indicated a wave is propagating parallel to the surface. (a) Sensitivity with

580 respect to a P-wave at different emerging angles of horizontal DAS (red) and geophone z-component

581 (blue). (b) Sensitivity with respect to an SV-wave at different emerging angles of horizontal DAS

582 (red) and geophone x-component (blue).

583 4 Siler and Faulds (2013) fault density mapping within the PoroTomo Survey box. This

584 model was used as a reflectivity model for the experiments within this section.

585 5 Reflectivity model from Siler and Faulds (2013) extracted at the location of Well 56-A1

586 used for simulating data. Blue dots represent source locations and the red dots represent geophone

587 locations. DAS fiber was placed between the geophone locations.

588 6 (a) Resulting image from migrating geophone synthetic data. (b) Resulting image from

589 migrating DAS synthetic data. (c) Combined image from migrating DAS and geophone synthetic

590 data.

591 7 Reflection amplitudes that represent the top 90% of energy recorded.

592 8 Inception v3 model architecture for one module modified from Szegedy et al. (2015). This
593 specific module performs filters on three pixel by three pixel as well as one pixel by one pixel sub-
594 sets of the original image. In parallel to these filters is a pooling layer that performs an operation
595 such as an average of all cells in subsets of the image.

596 9 (a) Examples of the automatically generated faults images used to train the CNN. (b) Ex-
597 amples of the automatically generated images that were not faults used to train the CNN.

598 10 Comparison between many velocity models extracted at Well 56-1A.

599 11 Body wave (P-wave) velocity (m/s) model from sweep interferometry in 3-D perspective
600 (Matzel et al., 2017b).

601 12 PoroTomo DAS survey geometry overlain by the vector direction (red) of the fiber at every
602 location.

603 13 Four layer model with a variety of structures used for data modeling. This model is used
604 as a density model for elastic modeling.

605

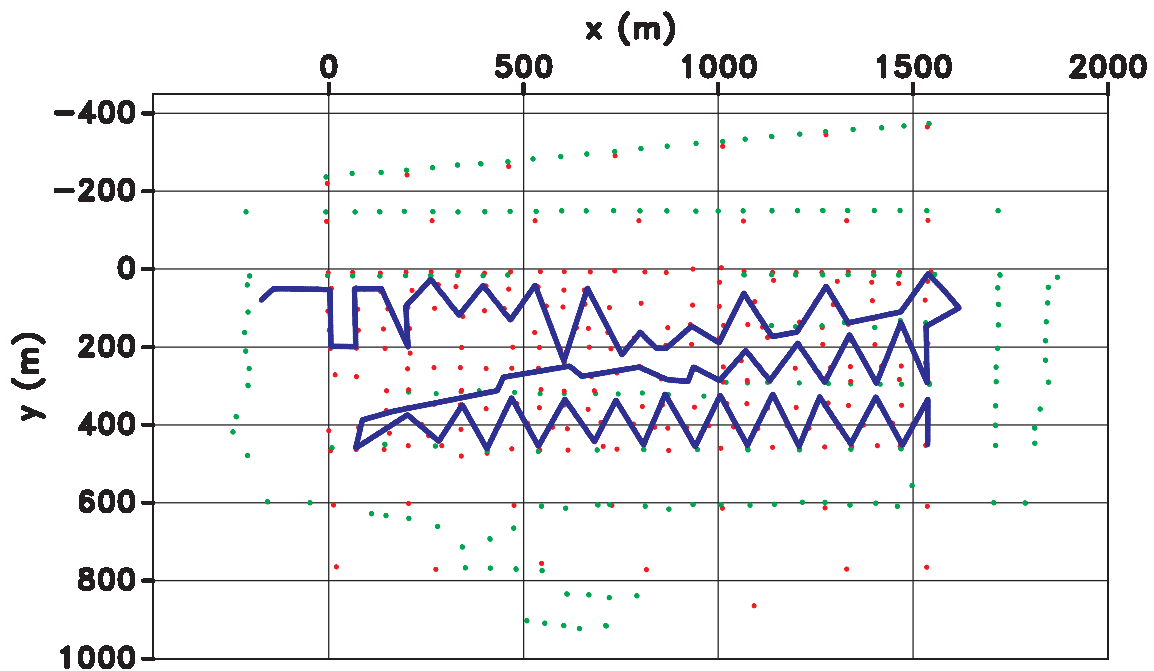
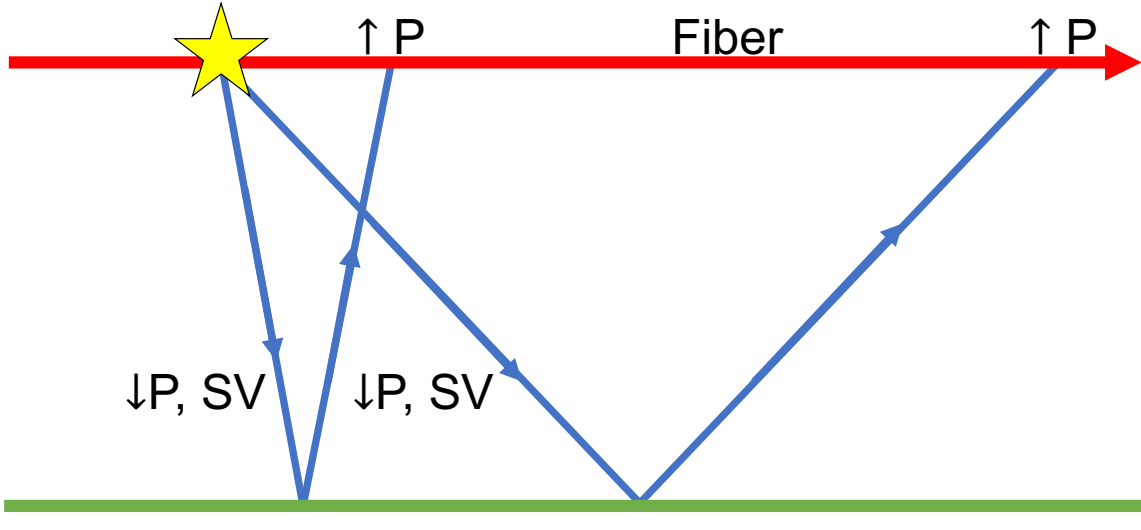
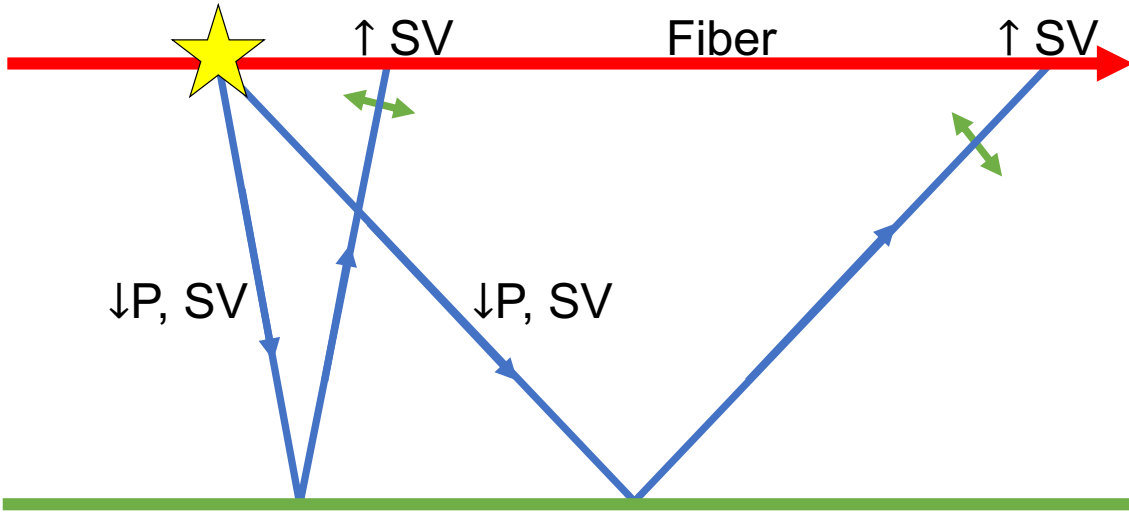


Figure 1: PoroTomo survey geometry. Green dots represent source locations, red dots represent geophone locations, and the blue line represents the surface DAS layout.

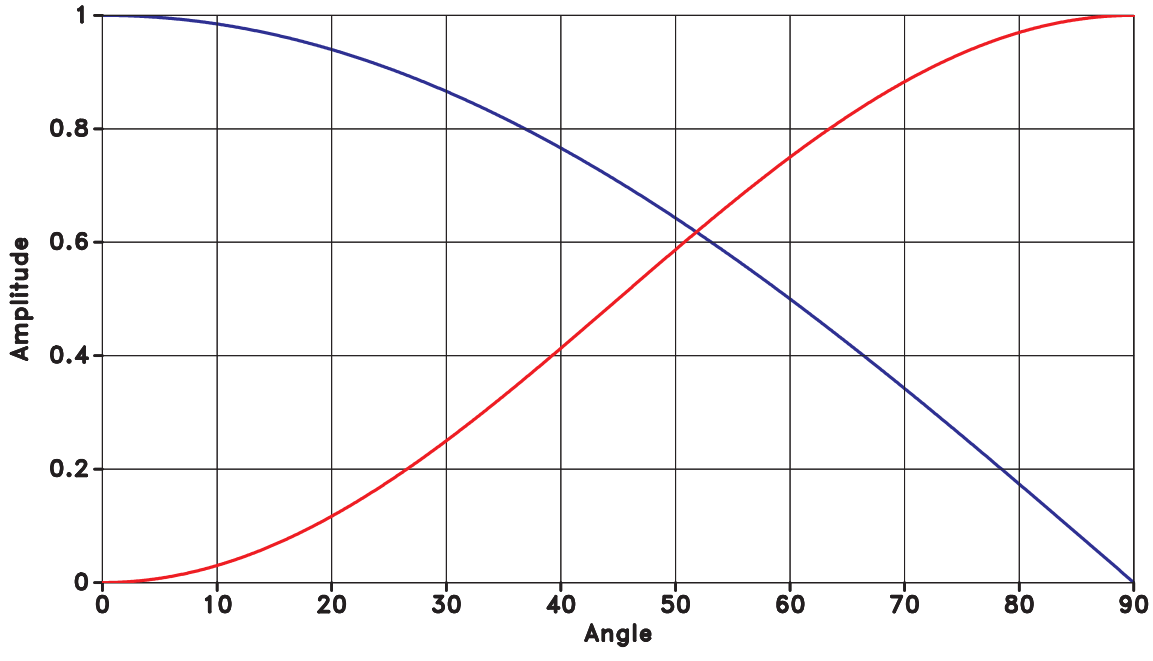


(a)

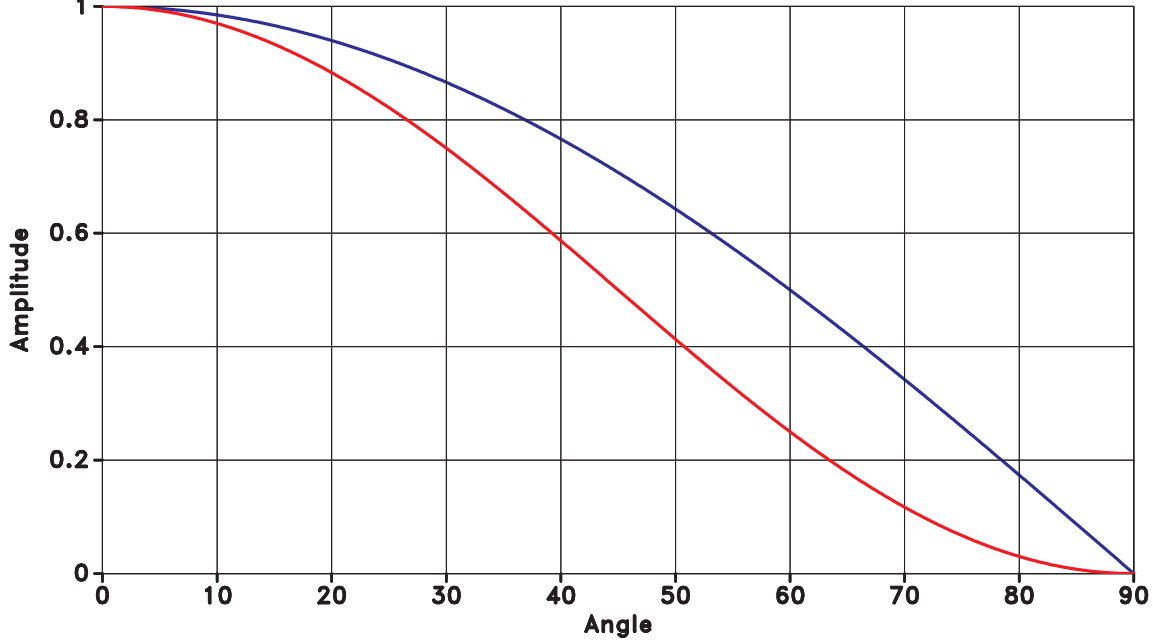


(b)

Figure 2: Consider a source that generates both P and S waves; this is a 2-D Homogeneous, flat-layered, isotropic ray path example. The blue lines represent ray paths of the labeled waves, the blue arrow represents the propagation direction of the wave, the green line represents a horizontal reflector in the subsurface, and the yellow star represents the source. (a) Demonstration of P-P wave effect on fiber using ray paths. Particle motion is inline with propagation direction (blue arrow). The fiber will only record data at large offsets. (b) Demonstration of P-SV wave effect on fiber using ray paths. Particle motion is perpendicular with the propagation direction (green arrows). The fiber will only record data at short offsets.



(a)



(b)

Figure 3: Amplitude versus emerging angle for both geophone (blue) and horizontal DAS (red). An emerging angle of 0° indicates a wave that is propagating perpendicular to the surface and an emerging angle of 90° degrees indicated a wave is propagating parallel to the surface. (a) Sensitivity with respect to a P-wave at different emerging angles of horizontal DAS (red) and geophone z-component (blue). (b) Sensitivity with respect to an SV-wave at different emerging angles of horizontal DAS (red) and geophone x-component (blue).

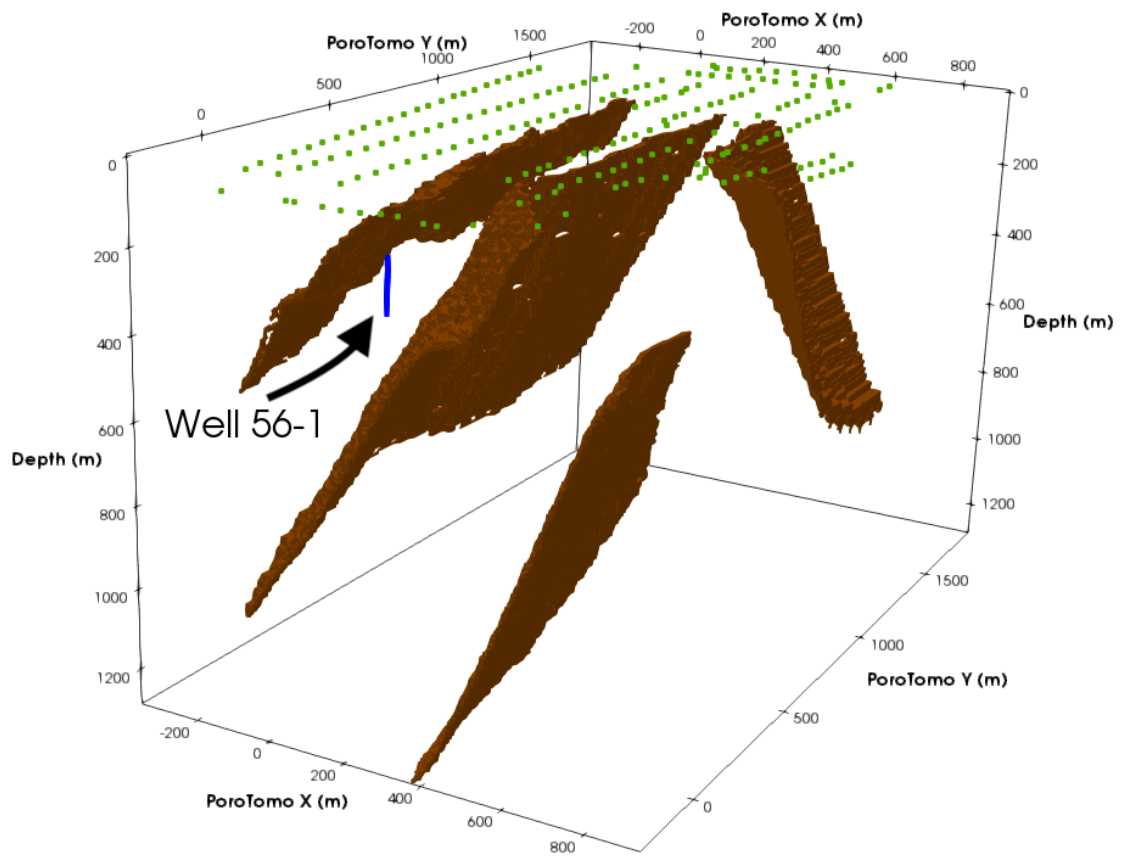


Figure 4: Siler and Faulds (2013) fault density mapping within the PoroTomo Survey box. This model was used as a reflectivity model for the experiments within this section.

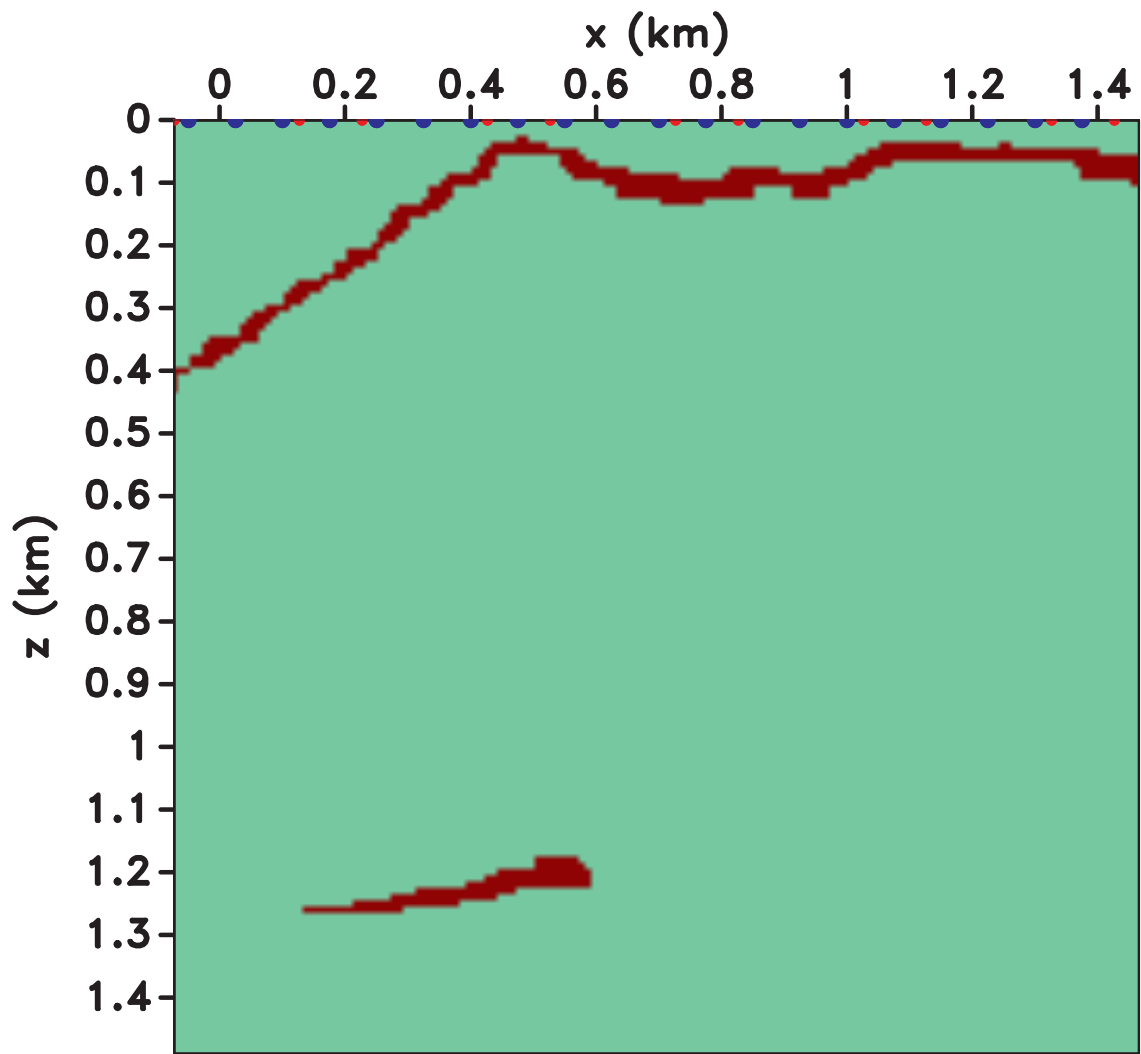


Figure 5: Reflectivity model from Siler and Faulds (2013) extracted at the location of Well 56-A1 used for simulating data. Blue dots represent source locations and the red dots represent geophone locations. DAS fiber was placed between the geophone locations.

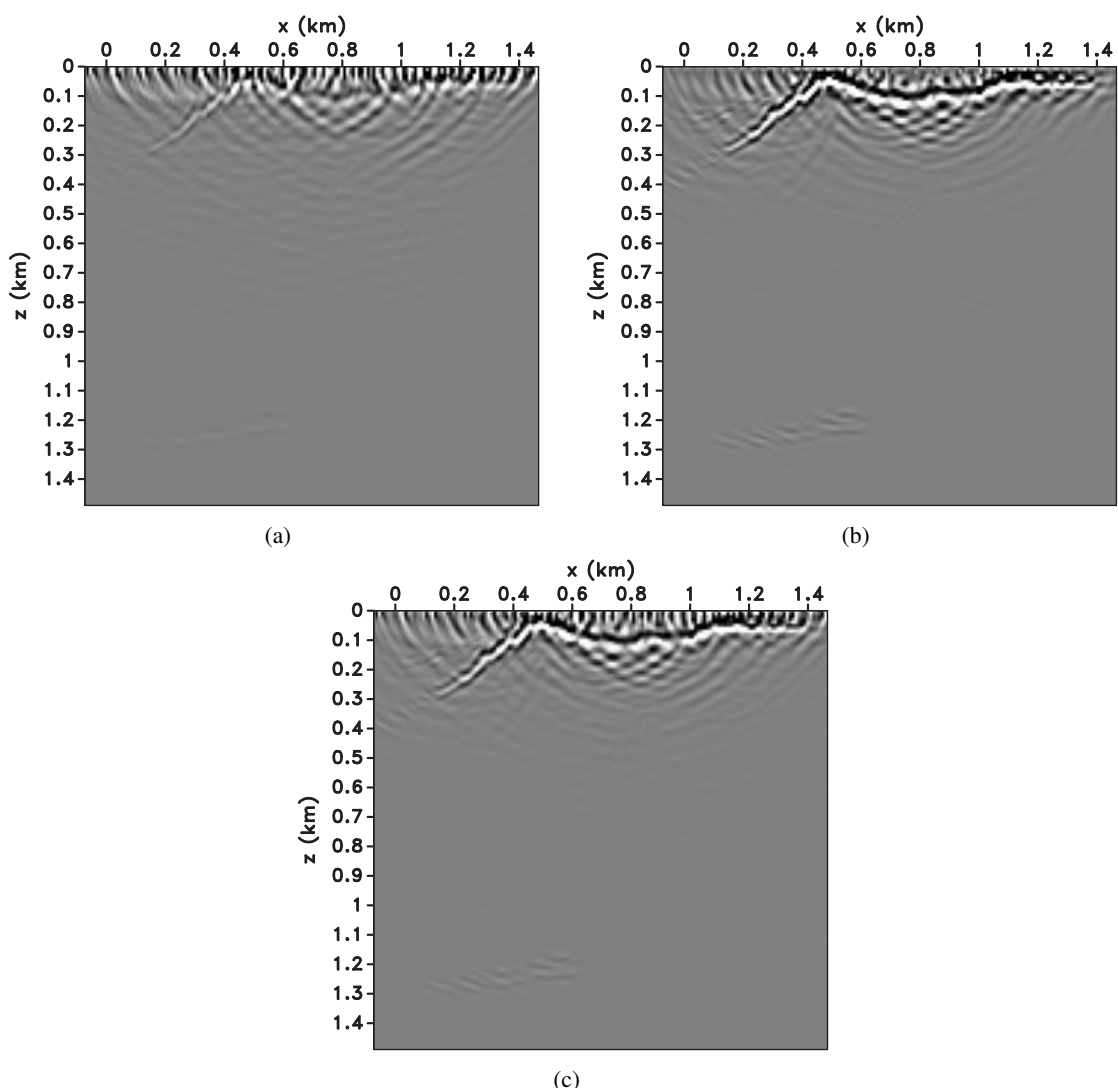


Figure 6: (a) Resulting image from migrating geophone synthetic data. (b) Resulting image from migrating DAS synthetic data. (c) Combined image from migrating DAS and geophone synthetic data.

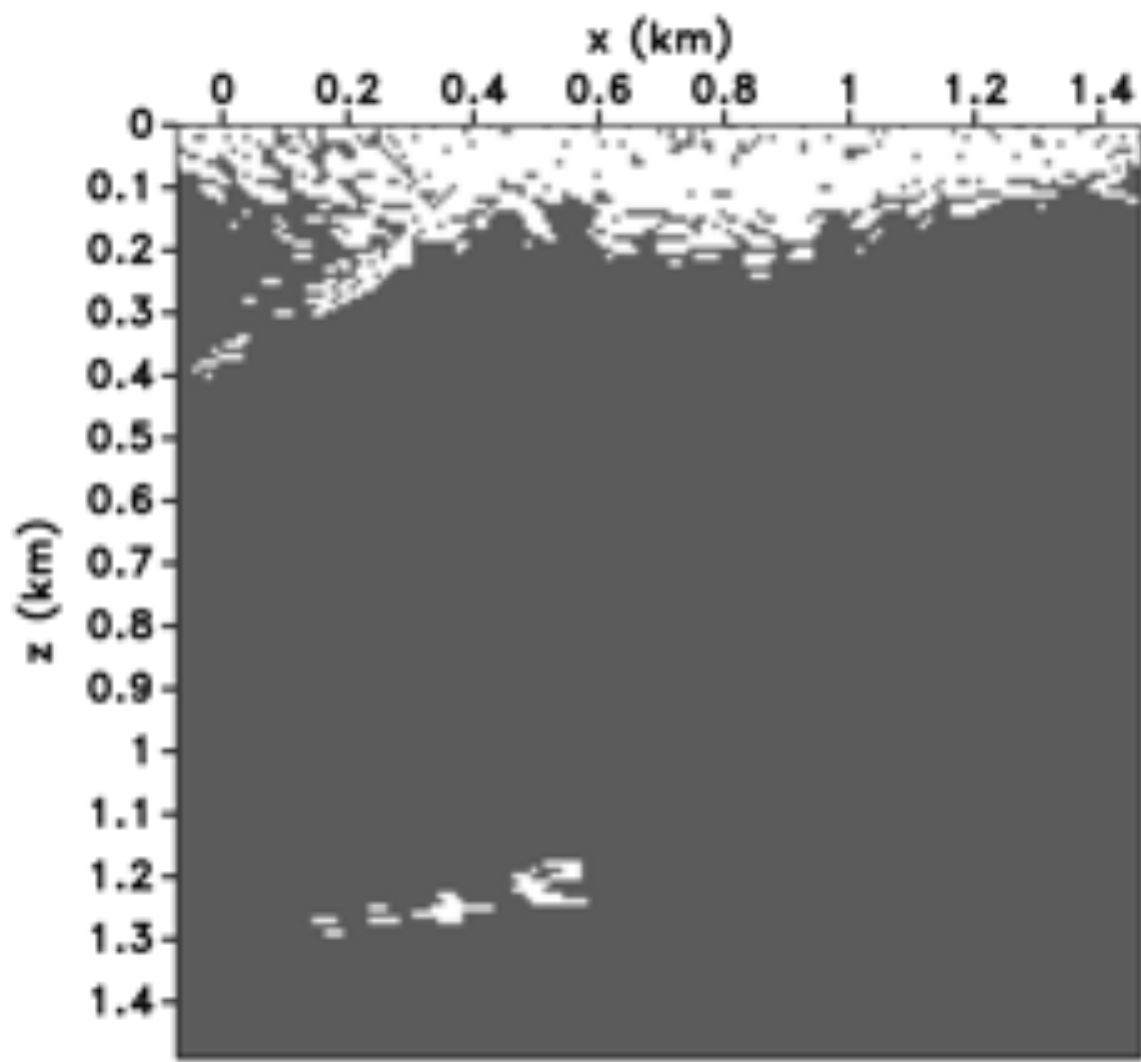


Figure 7: Reflection amplitudes that represent the top 90% of energy recorded.

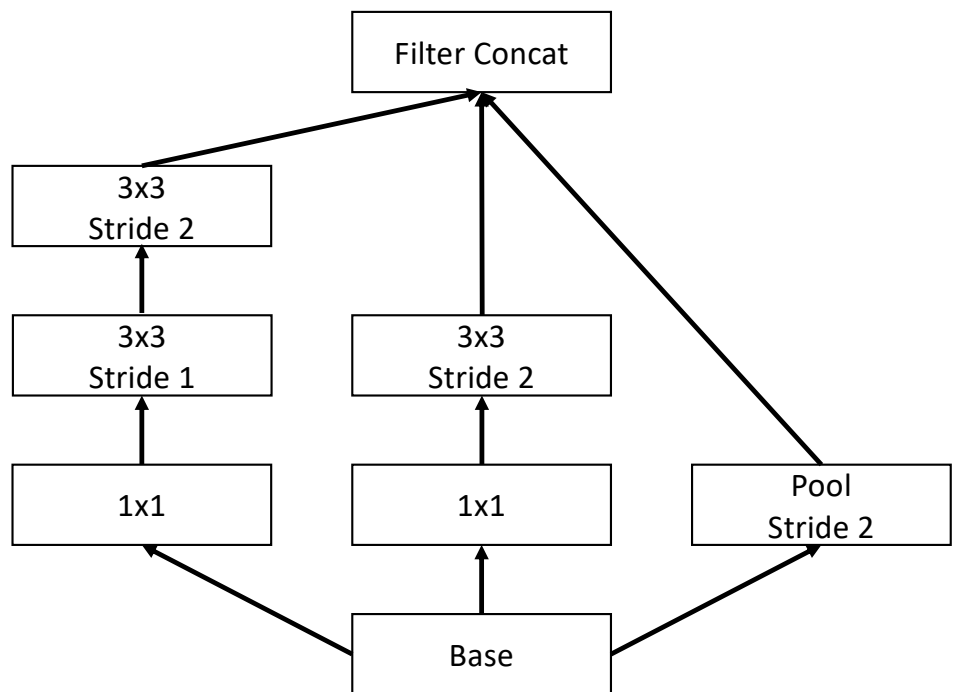
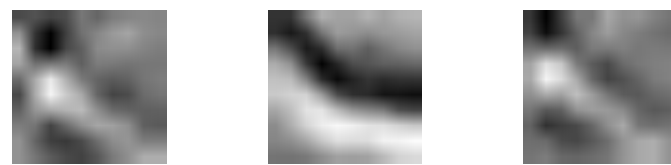
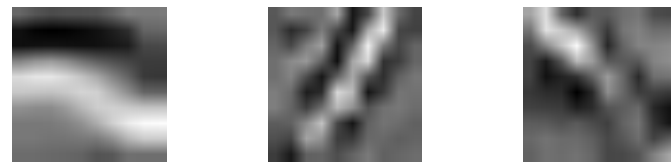
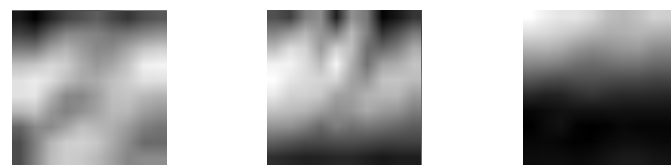


Figure 8: Inception v3 model architecture for one module modified from Szegedy et al. (2015). This specific module performs filters on three pixel by three pixel as well as one pixel by one pixel subsets of the original image. In parallel to these filters is a pooling layer that performs an operation such as an average of all cells in subsets of the image.



(a)



(b)

Figure 9: (a) Examples of the automatically generated faults images used to train the CNN. (b) Examples of the automatically generated images that were not faults used to train the CNN.

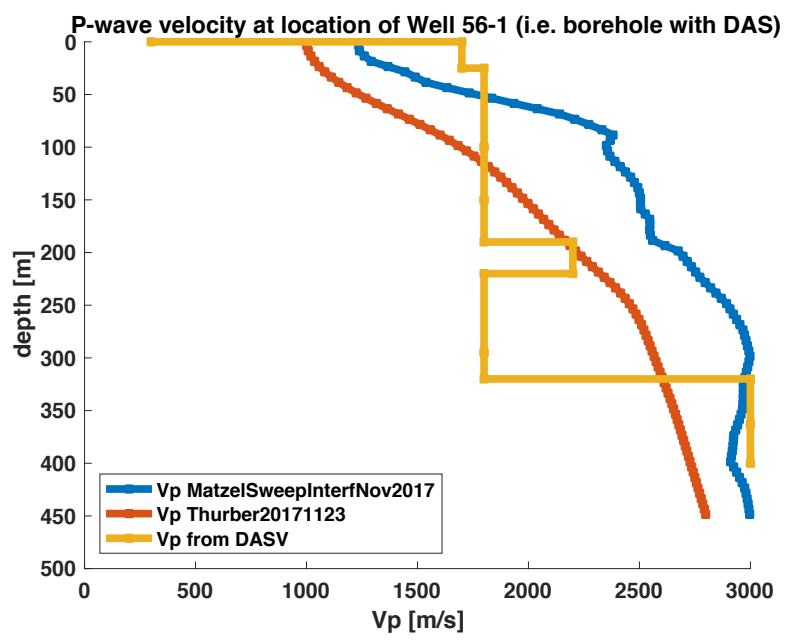


Figure 10: Comparison between many velocity models extracted at Well 56-1A.

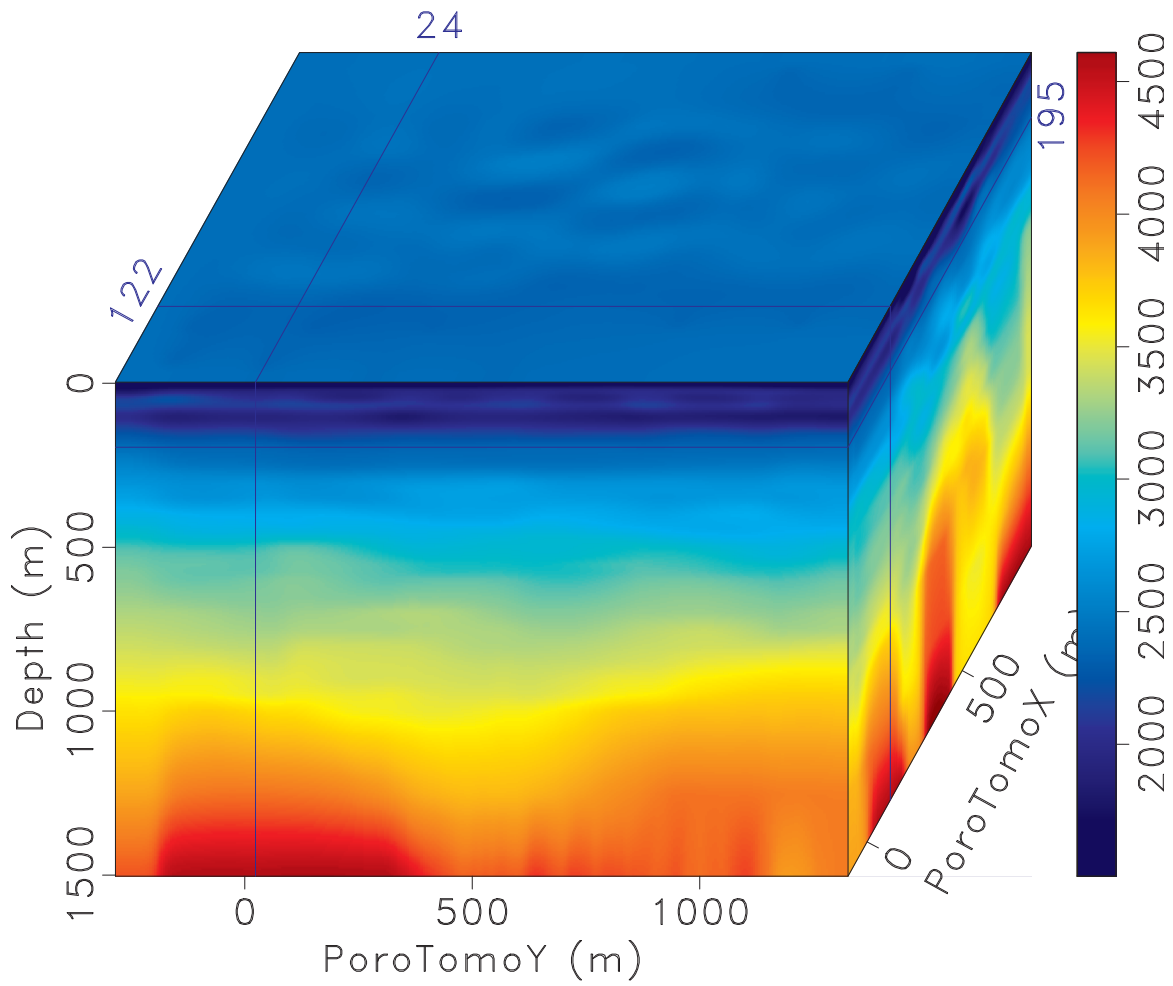


Figure 11: Body wave (P-wave) velocity (m/s) model from sweep interferometry in 3-D perspective (Matzel et al., 2017b).

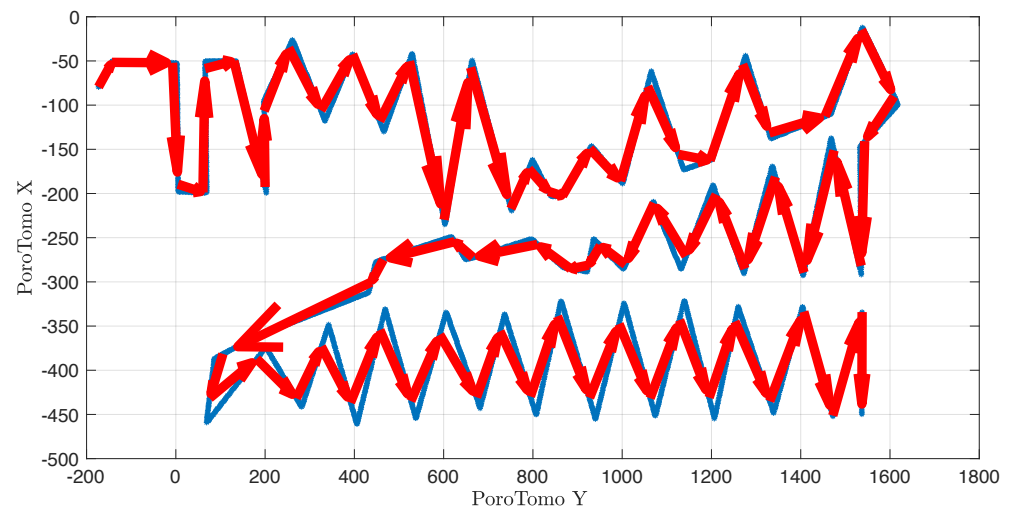


Figure 12: PoroTomo DAS survey geometry overlain by the vector direction (red) of the fiber at every location.

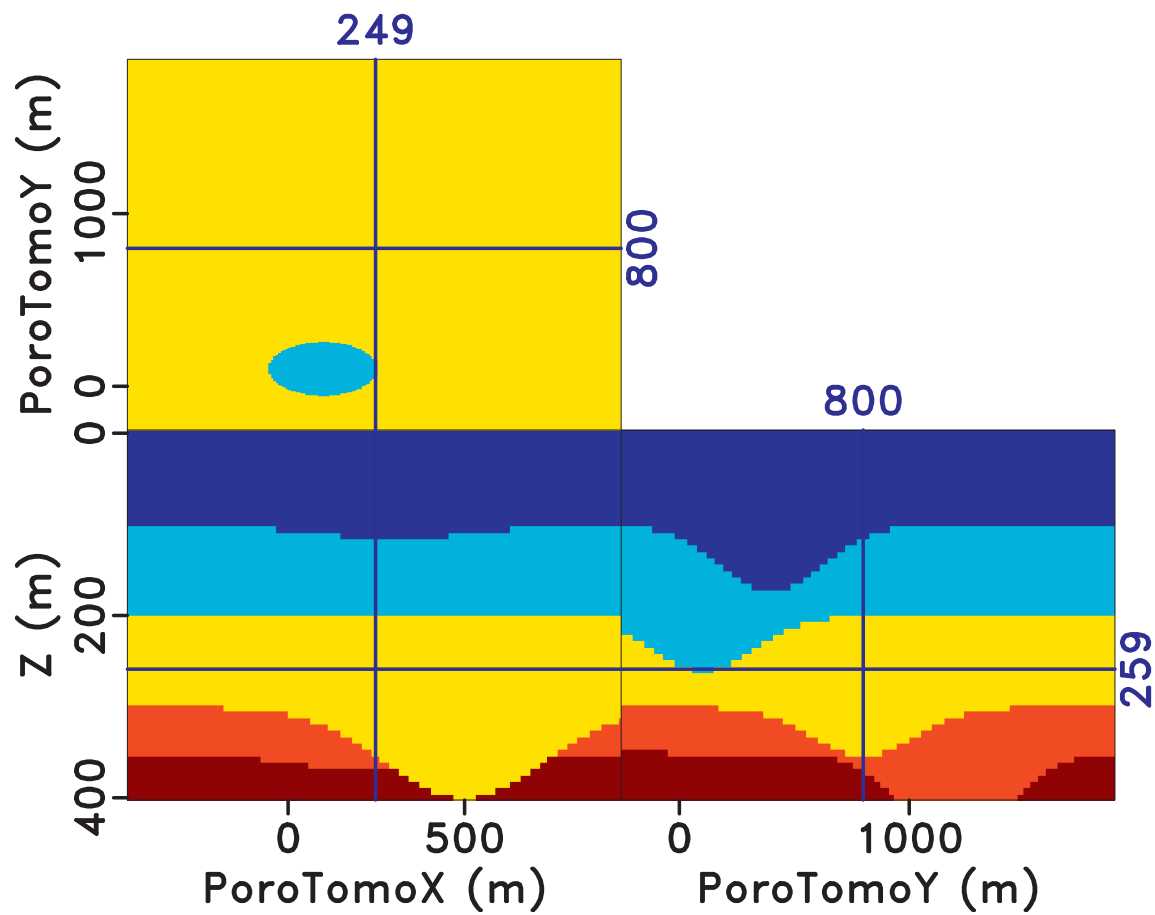


Figure 13: Four layer model with a variety of structures used for data modeling. This model is used as a density model for elastic modeling.